Sliding-impact bistable triboelectric nanogenerator for enhancing energy harvesting from low-frequency intrawell oscillation

Dongguo Tan[a], Jiaxi Zhou[a,*], Kai Wang[a, b,*], Huajiang Ouyang[c], Huai Zhao[c], Daolin Xu[a]

[a] *College of Mechanical and Vehicle Engineering, Hunan University, Changsha 410082, PR China*

[b] *Research Institute of Hunan University in Chongqing, Chongqing 401133, PR China*

[c] *School of Engineering, University of Liverpool, Liverpool L69 3GH, UK*

Abstract

A sliding-mode bistable triboelectric nanogenerator (SBTENG) has already been proven to be highly efficient for harvesting energy from low-frequency vibration. However, a SBTENG would undergo low-amplitude intrawell oscillation and thus output low power, if the excitation is weak. To enhance the efficiency of harvesting energy from low-frequency intrawell oscillation, a novel sliding-impact bistable TENG (SIBTENG) is proposed. The sliding-mode component of the SIBTENG enables energy harvesting from interwell oscillation effectively, while the impact-mode structure plays a vital role in enhancing energy harvesting from intrawell oscillation. The equation of motion of the SIBTENG is derived using Hamilton's principle and then numerically solved to obtain the dynamic responses. Subsequently, the output performance of the SIBTENG is evaluated by solving the electrical equation, which is unidirectional coupled to the equation of motion. Finally, experiments on the prototype of the SIBTENG are conducted to verify this design

* Corresponding author.
Address: College of Mechanical and Vehicle Engineering, Hunan University, Changsha 410082, PR China.
E-mail address: jxizhou@hnu.edu.cn (Jiaxi Zhou); Telephone number: +86 13975835883.
* Corresponding author.
Address: College of Mechanical and Vehicle Engineering, Hunan University, Changsha 410082, PR China.
E-mail address: wangkai@hnu.edu.cn (Kai Wang); Telephone number: +86 18011510813.

concept, which indicates good consistency between the theoretical and experimental results. Importantly, the impact-mode structure can notably enhance energy harvesting from intrawell oscillation. The output power of the devised SIBTENG is improved by about 100% over the SBTENG when they experience intrawell oscillation. The SIBTENG thereby enables high-efficiency energy harvesting whatever the oscillation pattern is.

Keywords: Energy harvesting, low-frequency vibration, sliding-impact mode, bistability, triboelectric nanogenerator.

1 Introduction

In the last few decades, wireless sensor network (WSN) has been widely used with the high-speed development of the internet of things (IoT). However, it is difficult for the traditional technology to power large WSNs because of its high installation and maintenance cost. How to power a wide range of WSNs, therefore, becomes an urgent problem to be solved in the development of IoT. An effective utilization of renewable energy such as wind energy [1–3], water energy [4–6] and vibration energy [7–9] in the environment provides a new mean for WSN energy supply. In fact, many energy harvesting technologies have been developed to convert these renewable energies into electrical one, such as piezoelectric mechanisms [10–13], electromagnetic mechanisms [14,15], pyroelectric mechanisms [16] and electrostatic mechanisms [17,18].

As an implementation of a burgeoning energy harvesting technology, triboelectric nanogenerators (TENGs) were first introduced by Wang et al. [19] in 2012. Subsequently, TENGs quickly attracted the attention of researchers worldwide owing to their distinct advantages of low cost in materials, suitability to low-frequency vibration sources and widespread applicability. After nearly 10 years of rapid development, TENGs can operate in four modes: in-plane sliding mode [20–22], vertical contact-separation mode [23–25], freestanding triboelectric-layer mode

[26–28] and single-electrode mode [29–31]. To evaluate the electrical output performance of these modes, the electric dynamics models were constructed by Niu et al. [25,32], and the relationship between the output performance and TENG parameters were investigated in-depth. For all types of TENGs, the output voltages of TENGs can be described by the relationship of *V* (voltage)-*Q* (transferred charges)-*x* (separation distance between electrodes) [33]. Based on this principle, various types of TENGs have been developed [34–37]. For example, Kim et al. [38] reported a collectively exhaustive hybrid TENG based on an impacting-sliding cylinder, which utilized both the sliding and contact-separation modes. Up to now, the TENGs have exhibited great potential in harvesting wind energy [39], ocean energy [40], vibration energy [41] and biomechanical energy [42].

Compared with other types of energies, vibration energy is ubiquitous in mechanical systems and engineering structures. To date, many elaborately structured TENGs have been proposed to harvest the vibration energy [43–47]. However, vibration in the environment is mostly dominated by low-frequency harmonics, and it is difficult to harvest energy from low-frequency vibration. To enhance the efficiency of energy harvesting from low-frequency vibration, a variety of TENGs have been designed and studied [48–50]. Generally, these TENGs can be categorized into three types. Firstly, it is a direct method to improve the electrical output by developing high-quality membranes, e.g. by combining the conductive fabric with a polydimethylsiloxane (PDMS) layer containing graphene oxide (GO) [51]. Secondly, it has been demonstrated that reducing the internal resistance can enhance the electrical performance of TENGs [52]. In addition, it is also an effective way to improve the electrical performance through manipulating its dynamic behaviours. For example, a quasi-zero-stiffness TENG was devised to achieve large-amplitude responses by triggering complicated dynamic behaviours, and thereby, to fulfill high-efficiency energy harvesting in a low-frequency region [53,54]. Consequently, it is also a feasible way to improve energy harvesting efficiency to engineer nonlinear structural configuration of TENGs.

The nonlinear energy harvesting system can efficiently harvest energy from

low-frequency vibration and broaden the bandwidth of energy harvesting. As a typical nonlinear system, the bistable system has two stable nodes and one unstable saddle point. When the proof mass of a harvester crosses the unstable saddle point (potential energy barrier), a snapping through phenomena happens, leading to interwell oscillation with large-amplitude displacement and high velocity [55]. In other words, the small-amplitude and low-velocity motion can be converted into large-amplitude and high-velocity motion by the beneficial snapping through phenomena. Based on this principle, many bistable TENGs have been proposed [56–59] to generate high electrical output. A TENG in the form of a cantilever beam with multistability was investigated theoretically, and the results showed that the performance of the TENG is excellent when the system exhibits interwell oscillation [33]. A disc-shaped bistable TENG was also reported, and it was demonstrated that this TENG was able to harvest continuous rotation and vibration energy in a low-frequency region [60]. Nevertheless, in a bistable system, the motion is usually dominated by intrawell oscillation, when the kinetic energy of the proof mass is not sufficiently large to enable it to cross the unstable saddle point. In such a motion state, there is still big room for improving energy harvest. In our previous work [61], a bow-type bistable TENG was designed, and it could achieved good electrical output performance in a low-frequency region when the TENG exhibited interwell oscillation. However, there was a sharp decrease in the output power of the TENG, when the motion pattern changed from interwell oscillation to intrawell one. Therefore, how to enhance the efficiency of harvesting energy from intrawell oscillation is an important issue to be addressed for a bistable TENG.

The main contribution of this study is to enhance the energy harvesting efficiency of a new bistable TENG when it experiences intrawell oscillation in a sliding-impact bistable TENG (SIBTENG). The novelty of the SIBTENG lies in using impact mechanism to improve energy harvesting efficiency during intrawell oscillation. High output power can be generated by the SIBTENG even when the proof mass cannot cross the potential energy barrier and the motion is dominated by intrawell oscillation. This superiority over the traditional SBTENG definitely benefits

from the introduction of the impact mechanism. To deeply study the relationship between the dynamic behaviours and electrical output of the SIBTENG, equations for both vibration and electrical charges are analytically derived and numerically solved. Furthermore, the effects of system parameters on both the dynamic and electrical responses are investigated as well. Finally, a prototype of the SIBTENG is manufactured and tested to validate the theoretical results.

This paper is organized as follows. In Section 2, the fundamental structure and the operation mechanism of the SIBTENG are presented in detail. The mechanical and electrical equations are established. The static features and dynamic behaviours of the SIBTENG are also presented in this section. In Section 3, the output performance of the SIBTENG is investigated. The effects of the system parameters on both the mechanical and electrical responses of the SIBTENG are discussed in Section 4. In Section 5, the experiments are carried out to validate the theoretical predications. Finally, some conclusions are drawn in Section 6.

2 Design and modeling

2.1 Conceptual design

The proposed SIBTENG includes two main parts, namely, the bistable structure and the energy harvesting unit, as shown in Fig. 1. The major role of the bistable structure is to impel the SIBTENG to oscillate, while the energy harvesting unit is utilized to convert the mechanical energy into electrical energy. It is worth noting that there are two modes for energy harvesting in this harvester, namely sliding and impact modes, as illustrated in Fig. 1a. The geometric parameters of the SIBTENG can be seen in Fig. 1b. The TENG is composed of a base plate, two flexible copper beams, two rigid rods, a proof mass, a polylactic acid (PLA) slider, a PLA guide rail and two stoppers. Additionally, Cu films (as the electrode) and fluorinated ethylene propylene (FEP) membranes (as the dielectric) are stuck to the slider, guide rail and stoppers, respectively, as illustrated in Fig. 1c. Moreover, Fig. 1c also shows the simplified

model of the energy harvesting unit. During operation, the slider slides upon the guide rail, and impact events happen between the slider and stopper.

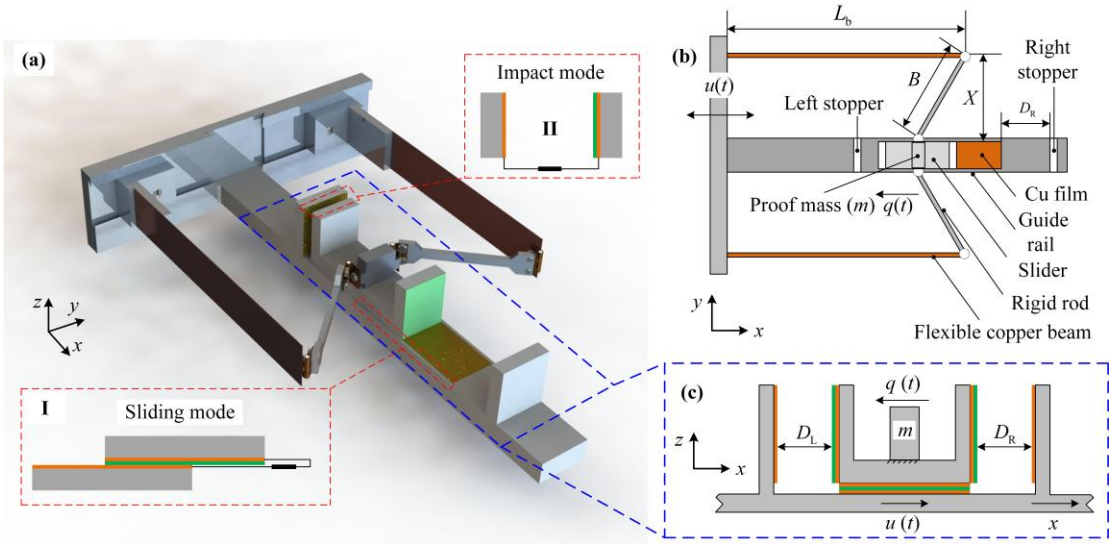

Fig. 1 Architecture of the SIBTENG. (a) Configuration of the SIBTENG and the modes of the energy harvesting; (b) components of the SIBTENG; (c) simplified dynamic model of the energy harvesting unit.

The operating mechanism [30] of the sliding mode is shown in Fig. 2a. The FEP membrane and Cu film of the SIBTENG are electrically charged owing to the electrostatic induction. In the initial state of the TENG, the FEP membrane and the Cu film fully overlap with each other, as shown in Fig. 2a-I. The FEP membrane gains electrons and the bottom Cu film loses electrons due to different ability of attracting electrons. However, there is no current flowing in the external circuit at the initial state, owing to zero potential between the FEP membrane and the Cu film. When the FEP membrane slides out of the bottom Cu film, as shown in Fig. 2a-II, the electrons are driven by electric potential difference (Fig. 2b) to flow from the top Cu film to bottom Cu film, and an instantaneous current is generated in the external circuit. Obviously, the electric potential difference notably increases as the FEP membrane slides on the bottom Cu film from the position shown in Fig. 2b-① to that in Fig. 2b-③. Therefore, the electrons flow from low potential to high potential, once the top Cu film is connected with the bottom Cu film through an external circuit.

After the FEP membrane slides to the limit position, as shown in Fig. 2a-III, it slides back in the opposite direction. In this case, the electrons flow from the bottom Cu film to the top Cu film, as depicted in Fig. 2a-IV, and the current flows from the top Cu film to bottom Cu film. The FEP membrane slides back when it slides to the limit position. Finally, the films fully overlap with each other, as shown in Fig. 2a-I. When the SIBTENG is in operating state, the FEP membrane periodically slides forward and backward on the bottom Cu film, and thus an alternating current (AC) can be generated in the external circuit.

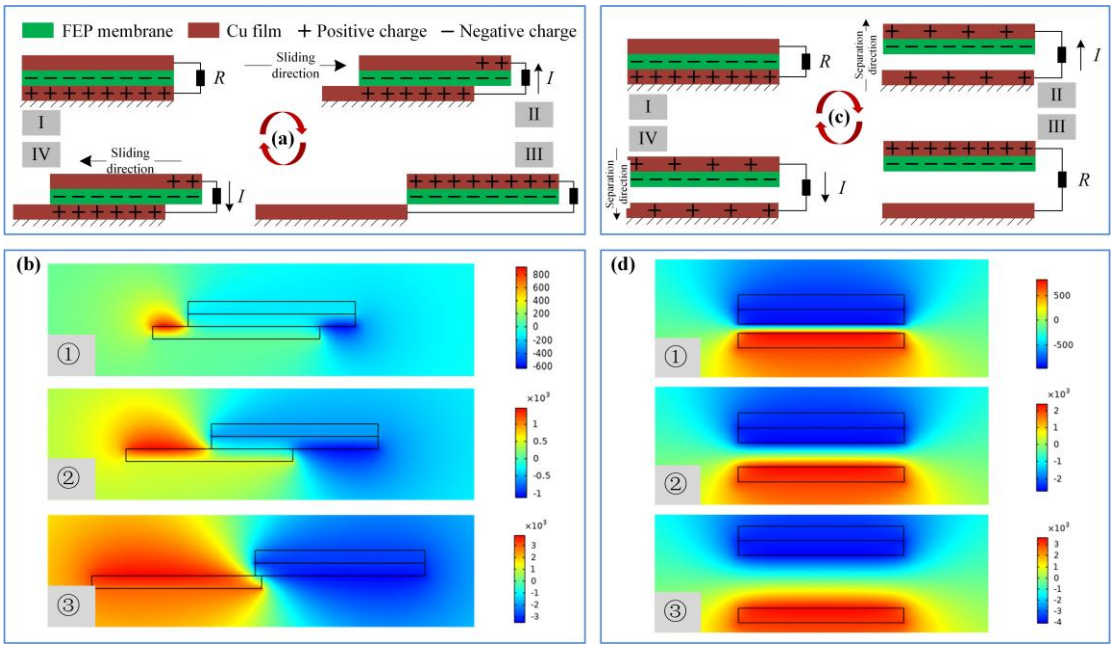

Fig. 2 Fundamental mechanisms. (a) Electron transfer of the sliding mode, (b) electric potential distributions of the sliding mode; (c) electron transfer of the impact mode, (d) electric potential distributions of the impact mode.

The operating mechanism [23] of the impact mode is shown in Fig. 2c. Firstly, the FEP membrane fully overlaps with the bottom Cu film (Fig. 2c-I), and no electrons transfer happens, since the potential difference is zero. Once the FEP membrane separates from the bottom Cu film, nonzero potential difference occurs. It drives the electrons to flow from the top Cu film to the bottom Cu film, and the current is generated, as depicted in Fig. 2c-II. Once the separation distance reaches the maximum, as shown in Fig. 2c-III, the FEP membrane moves in reverse, and the

separation distance between the FEP membrane and Cu film decreases. It results in opposite flow of the electrons, as shown in Fig. 2c-IV, owing to the decrease in potential difference. Consequently, the impact-mode structure also can generate an alternating current when the SIBTENG is in operating state.

2.2 Mechanical modeling

Based upon the extended Hamilton principle, the general variational equation of the mechanical system can be given as follows:

$$\delta\int_{t_1}^{t_2}(T-U)\mathrm{d}t+\int_{t_1}^{t_2}\delta W\mathrm{d}t=0 \tag{1}$$

where δ denotes the infinitesimal variation. T and U stand for the kinetic energy and potential energy, respectively. To be specific, the kinetic energy consists of three components (T_1, T_2 and T_3), namely, the kinetic energy of two flexible cantilevers, the kinetic energy of two rigid rods and the kinetic energy of the proof mass. W is the work done by the friction force F_f and the electrostatic force F_e. Additionally, t_1 and t_2 are the start and end time of the excitation, respectively.

The kinetic energy of two flexible beams can be evaluated by:

$$T_1=\int_0^{L_\mathrm{b}}\rho_\mathrm{b}b_\mathrm{b}h_\mathrm{b}\left[\frac{\partial w(x,t)}{\partial t}\right]^2\mathrm{d}x \tag{2}$$

where L_b, b_b and h_b denote the length, width and height of the elastic beam, respectively. ρ_b is the density of the beam. $w(x,t)$ stands for the transverse displacement of the beam.

The kinetic energy of two rigid rods can be given by:

$$T_2=m_\mathrm{b}v_\mathrm{b}^2+J\omega_\mathrm{b}^2 \tag{3}$$

where m_b is the mass of the rigid rod and v_b denotes the velocity of the center of mass, respectively. J and ω_b are the rotational inertia and the angular velocity of the rigid rod, respectively.

Assuming the tip velocity direction of the flexible copper beam is perpendicular to the velocity direction of the proof mass. The velocity and the angular velocity of the rigid rod can be expressed as follows:

$$v_{\mathrm{b}} = \frac{B\dot{z}(t)}{2\sqrt{B^2 - z^2(t)}} \tag{4}$$

$$\omega_{\mathrm{b}} = \frac{\dot{z}(t)}{\sqrt{B^2 - z^2(t)}} \tag{5}$$

where B is the length of the rigid rod. z denotes the relative displacement of the proof mass and can be given by:

$$z(t) = u(t) - q(t) \tag{6}$$

where $u(t)$ and $q(t)$ denote the base excitation and the response displacement of the proof mass, respectively.

The kinetic energy of the proof mass can be given by:

$$T_3 = \frac{1}{2} m\left[\dot{z}(t) - \dot{u}(t)\right]^2 \tag{7}$$

where m is the mass of the proof mass.

The elastic potential energy U of two flexible beams can be written as:

$$U = \int_0^{L_{\mathrm{b}}} EI\left[\frac{\partial^2 w(x,t)}{\partial x^2}\right]^2 \mathrm{d}x \tag{8}$$

where E is the Young's modulus and I denotes the second moment of the area of the beam's cross section.

For the flexible beam, the ratio of the length to the thickness is much larger than 10. The flexible beam is thereby considered as an Euler-Bernoulli beam, and only the bending deformation is taken into account for the theoretical analysis. In addition, the excitation frequencies (1 Hz-6 Hz) are much lower than the natural frequency of the first mode of the beams (102 Hz), therefore, the influences of the higher modes on the deformation of the beam can be neglected. The schematic diagram of the deformation progress of the flexible beams is shown in Fig. 3. The transverse displacement of the beam can be expressed as [62]:

$$w(x,t)=-\frac{Fx^2}{6EI}(3L_b-x)\quad(0\le x\le L_b) \tag{9}$$

where F is the force acting on the free end of the flexible beam, and L_b denotes the length of the beam.

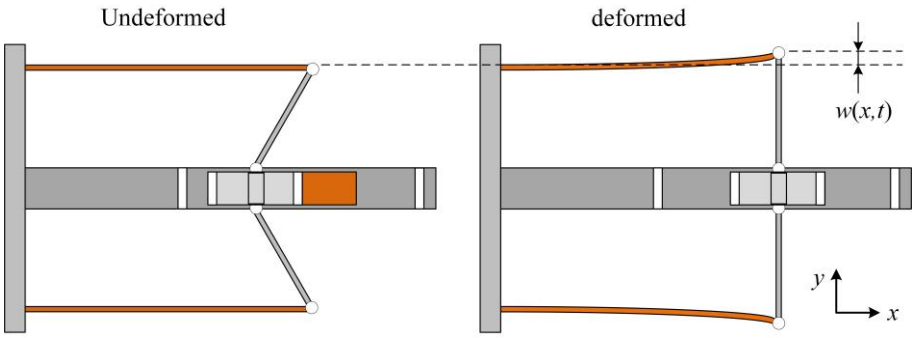

Fig. 3 Schematic diagram of the deformation progress of the flexible beams

According to the mechanics of materials [55], the expression between the force F and the deformation can be given by:

$$F=\frac{3EI}{L_b^3}\left(\sqrt{B^2-z^2(t)}-X\right) \tag{10}$$

where X denotes the distance between the elastic beam and the proof mass. Substituting Eq. (10) into Eq. (9), the transverse displacement can be rewritten as:

$$w(x,t)=-\frac{x^2(3L_b-x)}{2L_b^3}\left(\sqrt{B^2-z^2(t)}-X\right) \tag{11}$$

The Lagrange function for the mechanical system can be written as:

$$L=T-U \tag{12}$$

The dynamical equation of the mechanical system can be evaluated by:

$$\frac{\mathrm{d}}{\mathrm{d}t}\left(\frac{\partial L}{\partial \dot{z}}\right)-\frac{\partial L}{\partial z}=F_f z \tag{13}$$

Substituting Eqs. (2), (3), (6)-(8) and (11) into Eq. (13), the dynamical equation of the SIBTENG can be derived as:

$$M\ddot{z}+F_1+F_2-F_3=M_1\ddot{u}+F_f z \tag{14}$$

where M denotes the equivalent mass, and it can be expressed as:

$$M=\int_0^{L_b}\rho_b b_b h_b\left[\frac{x^2\left(3L_b-x\right)}{2L_b^3}\right]^2\left[\frac{2z^2}{B^2-z^2}\right]\mathrm{d}x+\frac{\left(B^2m_b+4J\right)z}{4\left[B^2-z^2\right]}+m \tag{15}$$

F_1, F_2, and F_3 denote the resultant forces, which can be given by:

$$F_1=\int_0^{L_b}\rho_b b_b h_b\left[\frac{x^2\left(3L_b-x\right)}{2L_b^3}\right]^2\left[\frac{2z\dot{z}^2}{B^2-z^2}+\frac{2z^3\dot{z}^2}{\left[B^2-z^2\right]^2}\right]\mathrm{d}x \tag{16}$$

$$F_2=\frac{\left(B^2m_b+4J\right)z\dot{z}^2}{2\left[B^2-z^2\right]^2} \tag{17}$$

$$F_3=2\int_0^{L_b}EI\left(\frac{3L_b-3x}{L_b^3}\right)^2\left[\frac{\left(\sqrt{B^2-z^2}-X\right)z}{\sqrt{B^2-z^2}}\right]\mathrm{d}x \tag{18}$$

The electrostatic force between the FEP membrane and Cu film can be expressed as [33]:

$$F_e=\frac{Q^2}{2\varepsilon_0\varepsilon_{r1}S_1} \tag{19}$$

where S_1 is the contact area between the FEP membrane and Cu film. According to Ref. [33,60], the electrostatic force has little effect on the dynamic responses of the bistable TENG. Hence, the electrostatic force will be neglected in this work.

Friction plays an important role in the TENG [63]. According to the theory of equivalent viscous damping, the energy consumed by viscous damping in a period can be approximated as:

$$\Delta E=-\oint c\dot{z}dz=-\int_0^T c\left(\dot{z}\right)^2dt \tag{20}$$

Assuming that the response is harmonic when the system under harmonic base excitation, the relative displacement response of the proof mass can be given by:

$$z=Z\sin\left(\omega_n t+\phi\right) \tag{21}$$

where Z is the amplitude, ω_n and ϕ denote the angular frequency and initial phase, respectively.

Substituting Eq. (21) into Eq. (20), the energy consumed by viscous damping in a period can be rewritten as:

$$\Delta E = -c\omega_n^2 Z^2 \int_0^{2\pi/\omega_n} \cos^2\left(\omega_n t + \phi\right) dt = -\pi c \omega_n Z^2 \tag{22}$$

According to the theory of Coulomb damping, the kinetic friction force can be expressed as:

$$F_{\mathrm{f}} = \mu N \operatorname{sgn}\left(\dot{z}\right) \quad \text{when} \quad \dot{z} \neq 0 \tag{23}$$

where μ denotes the kinetic coefficient of friction between the FEP membrane and bottom Cu film, *N* is the normal force, and $\operatorname{sgn}(\cdot)$ stands for the signum function.

The energy consumed by kinetic friction force in a period can be given by:

$$\Delta E = -4\mu N Z \tag{24}$$

Combining Eq. (22) and Eq. (24), the equivalent viscous damping coefficient can be yielded:

$$c = \frac{4\mu N}{\pi \omega_n Z} \tag{25}$$

When the relative velocity $\dot{z}$ between the slider and guide rail is not equal to zero, and $D_{\mathrm{L}} = 0$ or $D_{\mathrm{R}} = 0$, impact events happen between the slider and stoppers. Here, t^- and t^+ denote the times of the states before and after impact. In addition, a coefficient of restitution $r \in [0,1]$ is introduced to measure the energy transferred during impact. Therefore, the velocities of the guild rail and the slider after impact can be expressed as:

$$\dot{u}\left(t^+\right) = \frac{M\left(1+r\right)}{M+M_{\mathrm{T}}}\dot{q}\left(t^-\right) + \frac{M_{\mathrm{T}} - rM}{M+M_{\mathrm{T}}}\dot{u}\left(t^-\right) \tag{26}$$

$$\dot{q}\left(t^+\right) = \frac{M_{\mathrm{T}} - rM}{M+M_{\mathrm{T}}}\dot{q}\left(t^-\right) + \frac{M\left(1+r\right)}{M+M_{\mathrm{T}}}\dot{u}\left(t^-\right) \tag{27}$$

where M_{T} is the total mass of the SIBTENG and the vibration system. Actually, the total mass M_{T} is far greater than the equivalent mass *M* of the system. Hence, Eq. (26) and Eq. (27) can be rewritten as:

$$\dot{u}\left(t^+\right) = \dot{u}\left(t^-\right) \tag{28}$$

$$\dot{q}\left(t^{+}\right)=\dot{u}\left(t^{-}\right)-r\left[\dot{u}\left(t^{-}\right)-\dot{q}\left(t^{-}\right)\right] \tag{29}$$

Combining Eq. (28) and Eq. (29), one can be obtained:

$$\dot{z}\left(t^{+}\right)=-r\dot{z}\left(t^{-}\right) \tag{30}$$

where $\dot{z}\left(t^{-}\right)$ and $\dot{z}\left(t^{+}\right)$ represent the relative velocities before and after impact, respectively.

2.3 Electrical modeling

When the SIBTENG is driven by a base excitation, the slider slides upon the guide rail. The impact event happens between the slider and the stoppers when the clearance between the slider and stopper is closed, i.e. $D_{\mathrm{L}}=0$ or $D_{\mathrm{R}}=0$. Therefore, the SIBTENG is able to harvest energy through in-plane sliding mode and impact mode. The governing equation for the electrical component of the SIBTENG can be expressed as [32]:

$$V=-\frac{Q}{C}+V_{\mathrm{OC}} \tag{31}$$

where V denotes the output voltage, and V_{OC} is the open circuit (OC) voltage. Q is the transferred charges when the SIBTENG is in operation. C denotes the equivalent capacitance of the SIBTENG.

For in-plane sliding mode, the equivalent capacitance of the sliding-mode TENG can be given by [32]:

$$C_{\mathrm{slip}}=\frac{\varepsilon_0\varepsilon_{\mathrm{r}}w_{\mathrm{FEP}}\left(l-z\right)}{d} \tag{32}$$

where ε_0 and ε_{r} denote the vacuum permittivity and the relative permittivity of the dielectric (FEP membrane), respectively. l, w_{FEP} and d represent the length, width and thickness of the FEP membrane, respectively. σ denotes the surface charge density of the TENG.

According to the Ref. [32], the electric field of the overlapped region between the FEP membrane and bottom Cu film can be expressed as:

$$E_{\text{slip}} = \frac{\sigma z}{\varepsilon_0 \varepsilon_{\text{r}} \left(l - z\right)} \tag{33}$$

where σ denotes the surface tribo-charge density.

The OC voltage of the sliding-mode TENG can be given by:

$$V_{\text{OC-slip}} = E_{\text{slip}} d = \frac{\sigma z}{\varepsilon_0 \left(l - z\right)} \frac{d}{\varepsilon_{\text{r}}} \tag{34}$$

Substituting Eqs. (32) and (34) into Eq. (31), the output voltage of the sliding-mode TENG can be expressed as:

$$V_{\text{slip}} = -\frac{Q}{w_{\text{FEP}} \varepsilon_0 \left(l - z\right)} \frac{d}{\varepsilon_{\text{r}}} + \frac{\sigma z}{\varepsilon_0 \left(l - z\right)} \frac{d}{\varepsilon_{\text{r}}} \tag{35}$$

According to the Ohm's law $V = IR = R\dfrac{\mathrm{d}Q}{\mathrm{d}t}$, the electrical differential equation of the sliding-mode TENG can be given by:

$$R\frac{\mathrm{d}Q}{\mathrm{d}t} = -\frac{Q}{w_{\text{FEP}} \varepsilon_0 \left(l - z\right)} \frac{d}{\varepsilon_{\text{r}}} + \frac{\sigma z}{\varepsilon_0 \left(l - z\right)} \frac{d}{\varepsilon_{\text{r}}} \tag{36}$$

Moreover, the equivalent capacitance and the OC voltage of the impact-mode TENG can be given by [25]:

$$C_{\text{cs}} = \frac{\varepsilon_0 S}{d_0 + D} \tag{37}$$

$$V_{\text{OC-cs}} = \frac{\sigma D}{\varepsilon_0} \tag{38}$$

where *S* stands for the contact area between the FEP membrane and Cu film when the impact event occurs. d_0 is the effective thickness of the FEP membrane which can be written as d/ε_{r}. *D* is the distance between the slider and stoppers. Specifically, $D = D_{\text{L}} + z$ when the impact event occurs between the slider and left stopper, while $D = D_{\text{R}} - z$ as the impact event happens between the slider and right stopper.

Substituting Eqs. (37) and (38) into Eq. (31), the output voltage of impact-mode TENG can be derived:

$$V_{cs} = -\frac{Q}{S\varepsilon_0}\left(d_0 + D\right) + \frac{\sigma D}{\varepsilon_0} \tag{39}$$

According to the Ohm's law $V = IR = R\frac{\mathrm{d}Q}{\mathrm{d}t}$, the electrical differential equation of the impact-mode TENG can be given by:

$$R\frac{\mathrm{d}Q}{\mathrm{d}t} = -\frac{Q}{S\varepsilon_0}\left(d_0 + D\right) + \frac{\sigma D}{\varepsilon_0} \tag{40}$$

Under continuous excitation, the electrical output voltage is time-dependent. The peak voltage and root mean square (RMS) voltage can be obtained. The output voltage and power are calculated by the summation of the voltages and powers generated through different types of energy harvesting modes [47], which are utilized to assess the performance of the SIBTENG.

2.4 Mechanical behaviours of the bistable structure

The bistable structure is the key component of the SIBTENG and its mechanical characteristics play a critical role in the energy harvesting efficiency. To clarify the effect of the mechanical behaviours on the electrical outputs of the SIBTENG, this section studies mechanical features of the bistable structure. The structural parameters of the SIBTENG are tabulated in Table 1. The subsequent numerical simulations are carried out using these parameters.

Table 1 Structural parameters of the SIBTENG

Parameter	Value
Density of the flexible beam ρ_b	8900 kg/m^3
Elasticity modulus of the flexible beam E	100 GPa
Cross section of the flexible beam $b_b \times h_b$	0.016 m×0.0003 m
Length of the flexible beam L_b	0.1 m
Length of the rigid rod B	0.04661 m
Mass of the proof mass m	0.0022 kg

Mass of the slider m_s	0.0031 kg
Mass of the rigid rod m_b	0.0018 kg
Kinetic friction coefficient μ	0.22
Coefficient of restitution r [47]	0.6

To understand the working mechanism of the SIBTENG, the mechanical behaviours, such as restoring force and potential energy, of the bistable structure are investigated, as shown in Fig. 4. In this proposed SIBTENG, the restoring force acting on the proof mass is induced by the flexible cantilever beams. It can be seen from Fig. 4a that the restoring force is remarkably affected by the distance between the flexible beam and the proof mass. Obviously, the negative stiffness at the static equilibrium point can be notably enhanced as the distance is reduced. Moreover, the elastic potential energy of the system is depicted in Fig. 4b, where a double-well feature can be clearly observed. It implies that the system possesses bistability. It also shows that the potential energy barrier gets higher as the distance between the flexible beam and the proof mass is reduced. Importantly, it is difficult for the proof mass to cross the potential energy barrier, and the motion of the proof mass is dominated by the intrawell oscillation, when the potential energy barrier is high corresponding to a small distance X. Once the proof mass crosses the potential barrier, the SIBTENG exhibits interwell oscillation. Therefore, the mechanical behaviours of the bistable structure can be tuned by changing the distance X.

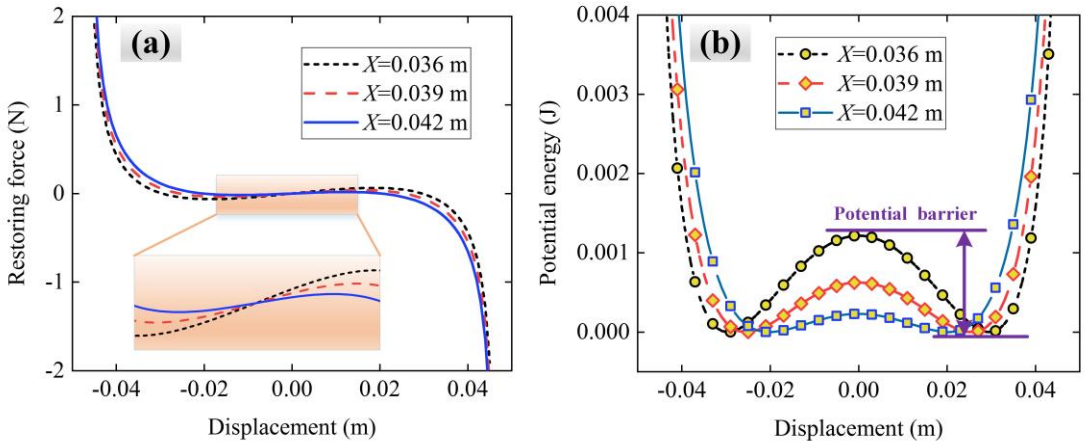

Fig. 4 Mechanical behaviours of the bistable structure. (a) Restoring force versus displacement, and (b) potential energy versus displacement for the horizontal distance between the flexible beam and the proof mass of 0.036 m, 0.039 m and 0.042 m.

2.5 Dynamic behaviours of the SIBTENG

The electrical performance of the SIBTENG is closely related to its dynamic behaviours. This section investigates the dynamic behaviours of the SIBTENG under different excitation frequencies. To calculate the dynamic responses, the distance X is selected as 0.042 m, the amplitude of the harmonic base excitation A is set to be 0.7 G (G=9.8 m^2/s). When the SIBTENG is in operating state, the dynamic responses of the SIBTENG are depicted in Fig. 5. Note that the distance between the right stopper and left stopper is 0.05 m. When the displacement of the proof mass reaches 0.025 m or -0.025 m and the velocity of the proof mass is not equal to zero, impact events happen between the slider and stoppers. Specifically, the slider is in contact with the stopper firstly and then the proof mass moves in reverse. The proof mass loses part of kinetic energy during impact event, and the displacement and velocity of the proof mass are reversed after impact event.

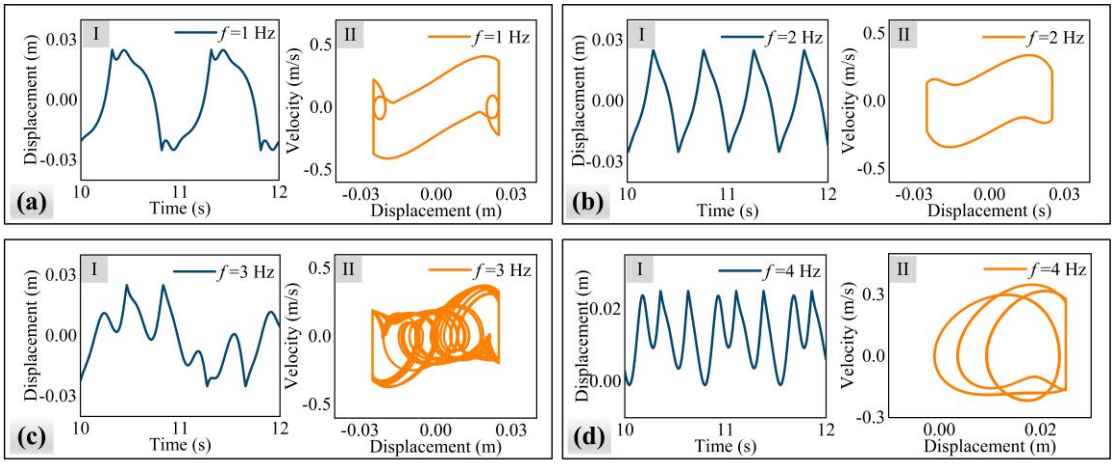

Fig. 5 Responses of the SIBTENG under an excitation with amplitude of A=0.7 G, and frequency of (a) 1 Hz, (b) 2 Hz, (c) 3 Hz and (d) 4 Hz, when the distance X between the proof mass and the flexible beam is 0.042 m.

As shown in Fig. 5a-I, the motion of the proof mass is interwell oscillation when the excitation frequency is 1 Hz. In this case, the proof mass crosses the potential barrier easily owing to the larger displacement amplitude of the base excitation. Clearly, when the proof mass reaches the absolute maximum displacement, impacts occur between the slider and stoppers, as illustrated in the phase portrait Fig. 5a-II. As the excitation frequency increases to 2 Hz, the proof mass also exhibits the interwell oscillation, as shown in Fig. 5b. When the frequency further increases to 3 Hz, the displacement amplitude of the base excitation decreases, which is unable to drive the proof mass to cross the potential barrier periodically. Therefore, the proof mass exhibits aperiodic interwell oscillation, and the impact events happen aperiodically. As depicted in Fig. 5d, the motion of the proof mass is dominated by the intrawell oscillation when the frequency is 4 Hz. The reason is that the displacement amplitude of the base excitation further decreases, and the proof mass cannot cross the potential barrier. It also can be observed that the impact events only happen between the slider and right stop in this case.

3 Output performance of the SIBTENG

This section investigates the electrical output performance of the SIBTENG. The output voltage of the SIBTENG is obtained by resolving the electrical equation that is unidirectional coupling to the dynamic equation. When the SIBTENG is in operating state, the slider slips on the guide rail and an electrical output is generated by sliding mode. Moreover, the impact events between the slider and stopper happen as the absolute value of displacement response of the proof mass is greater than 0.025 m, and the output voltage is generated through impact mode. The electrical parameters of the SIBTENG used in the following numerical simulations are listed in Table 2.

Table 2 Numerical simulation parameters of the SIBTENG

Parameter	Value
Thickness of FEP membrane d	3×10^{-5} m

Length of FEP membrane (sliding mode) l_s	0.04 m
Length of FEP membrane (impact mode) l_c	0.04 m
Width of FEP membrane w_{FEP}	0.04 m
Thickness of Cu film d_1	5×10^{-5} m
Length of Cu film (sliding mode) l_1	0.04 m
Length of Cu film (impact mode) l_2	0.04 m
Width of Cu film w_1	0.04 m
Relative permittivity of FEP membrane ε_r	4
Vacuum permittivity ε_0	8.85×10^{-12} F/m
Surface tribo-charge density σ	600 μC/m^2
Load resistance R	200 MΩ

To calculate the output voltages of the sliding mode and impact mode of the SIBTENG, the distance X and the excitation amplitude A are set as 0.042 m and 0.7 G. Fig. 6a shows the time histories of the voltage of the sliding mode as the excitation frequency varies from 1 Hz to 6 Hz. When the frequency is 1 Hz, the proof mass can cross the potential barrier easily, and the motion of the proof mass is periodic interwell oscillation. Thus, the output voltage of the sliding mode is also periodic and the voltage amplitude is high. As the frequency increases to 2 Hz, the voltage amplitude decreases a little. When the frequency increases to 3 Hz, the waveform of the output voltage is aperiodic. This is because the proof mass cannot periodically cross the potential barrier, and the motion of the proof mass becomes aperiodic interwell oscillation. As the frequency is further increased to 4 Hz, 5 Hz or 6 Hz, the proof mass exhibits intrawell oscillation, and the voltage amplitude decreases gradually. The reason is that the proof mass cannot cross the potential barrier, and thereby, the proof mass vibrates around a stable equilibrium point.

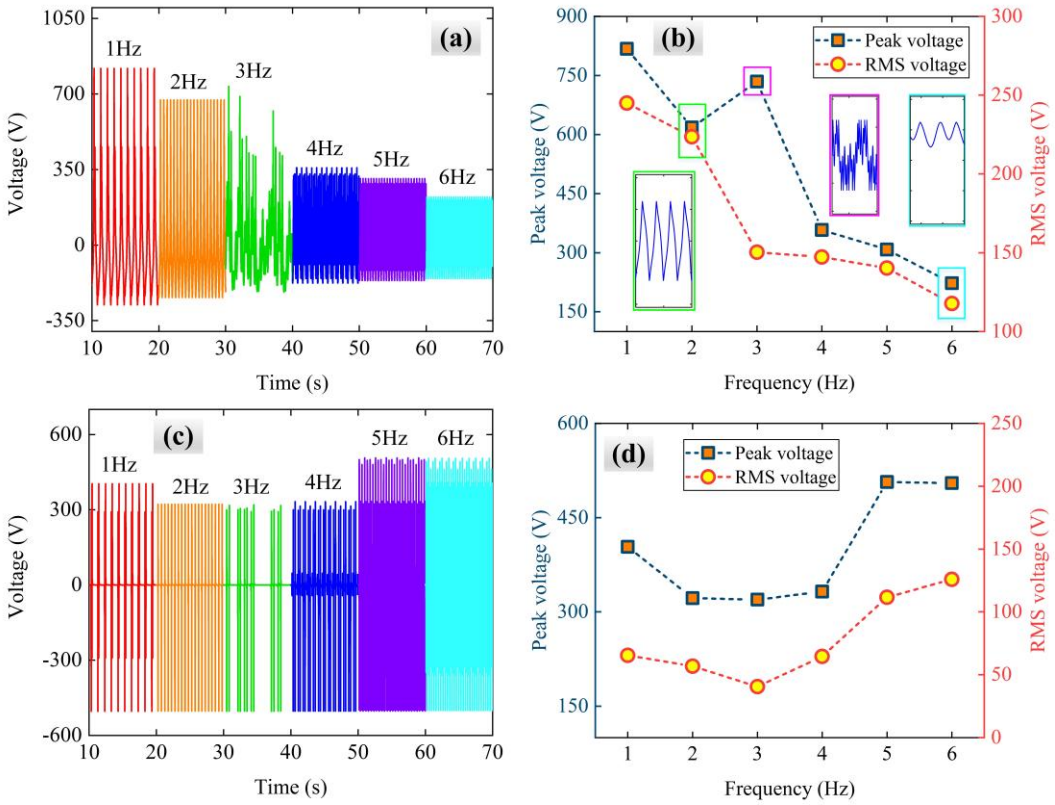

Fig. 6 Numerical output performance of the SIBTENG under an excitation with amplitude of A=0.7 G and the distance X=0.042 m. Sliding mode: (a) time histories of voltage for different excitation frequencies; (b) comparison of the peak voltage and RMS voltage outputs under different excitation frequencies. Impact mode: (c) time histories of voltage for different excitation frequencies; (d) comparison of the peak voltage and RMS voltage outputs under different excitation frequencies.

As depicted in Fig. 6b, the variation trends of the peak voltage and RMS voltage of the sliding mode are almost identical to each other. Obviously, both the peak voltage and RMS voltage gradually decrease as the frequency increases. However, the peak voltage at 3 Hz is higher than that at 2 Hz, due to larger peak displacement amplitude of the aperiodic interwell oscillation at the excitation frequency of 3 Hz. When the frequency is 4 Hz, 5Hz or 6 Hz, both the peak voltage and RMS voltage notably decline, since the proof mass undergoes intrawell oscillation in sliding mode.

When the impact event happens between the slider and right stopper, Fig. 6c shows the time histories of voltage for different excitation frequencies. The

comparison of the peak voltage and RMS voltage under different excitation frequencies is depicted in Fig. 6d. It can be seen that both the peak voltage and RMS voltage initially decrease and then increase with the excitation frequency. Obviously, the RMS voltage generated through impact mode under intrawell oscillation are higher than that under interwell oscillation. The reason is that the electrical output of the impact-mode component of the SIBTENG is mainly influenced by the separation velocity between the FEP membrane and Cu film. In the case of intrawell oscillation and the separation velocity is higher than that in the case of interwell oscillation. Therefore, high-efficient energy harvesting can be realized through impact-mode mechanism when the TENG undergoes intrawell oscillation.

Fig. 7 shows the comparison between the power generated by the sliding mode and the sliding-impact mode as the frequency varies from 1 Hz to 6 Hz. Here, the power growth rate is defined as $\frac{p_{s\text{-}c} - p_s}{p_s} \times 100\%$, where $p_{s\text{-}c}$ and p_s are the power of sliding-impact and sliding modes, respectively. As depicted in Fig. 7a, the peak power of the sliding-impact mode is larger than that of the sliding mode at each frequency. Clearly, the growth rate increases with the increase of frequency, and more importantly, when the SIBTENG undergoes intrawell oscillation, the growth rate is much higher than that in the case of interwell oscillation.

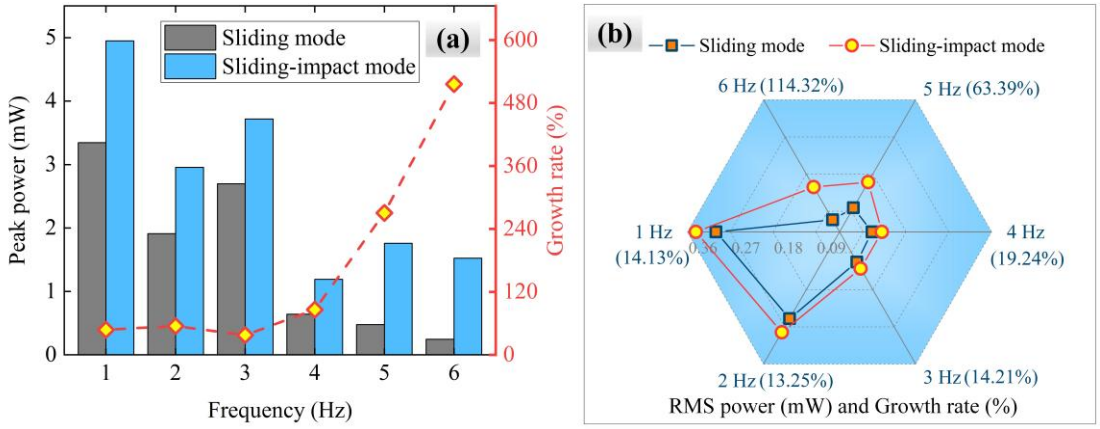

Fig. 7 Comparison of the power of the sliding mode and sliding-impact mode under different frequencies. (a) Peak power and the growth rate; (b) RMS power and the growth rate.

The RMS power is depicted in Fig. 7b, which has the same variation trend as the peak power. Note that the RMS powers generated by the impact mode at 5 Hz and 6 Hz are larger than those at 1 Hz and 2 Hz, since that the separation velocities of the films at 5 Hz and 6 Hz are faster than those at 1 Hz and 2 Hz. When the excitation frequencies are 1 Hz, 2 Hz and 3 Hz, the proof mass can cross the potential barrier and the SIBTENG exhibits interwell oscillation, and the growth rate of RMS power is about 14%. When the motion pattern of the proof mass changes from the interwell oscillation to the intrawell oscillation at 4 Hz, 5 Hz and 6 Hz, the growth rate increases to 19.24% at 4 Hz, 63.39% at 5 Hz and about 110% at 6 Hz. Therefore, the electrical output performance under intrawell oscillation can be effectively improved by introducing the impact mode into the bistable TENG. To further prove this advantage, Table 3 is given for comparing the performance of intrawell oscillation between the SIBTENG and other TENGs. It can be seen that the output power of intrawell oscillation of the SIBTENG is higher than that of other TENGs.

Table 3 Performance comparison of intrawell oscillation between the SIBTENG and other TENGs

Device dimensions	Frequency	Output power	Load Resistance	Ref.
50 mm × 16 mm	3.5 Hz	74 μW	110 MΩ	[61]
40 mm × 30 mm	4 Hz	0.1 μW	10 MΩ	[64]
70 mm × 70 mm	8 Hz	0.033 μW	11 MΩ	[65]
47 mm × 20 mm	10 Hz	8.58 μW	35 MΩ	[66]
40 mm × 40 mm	6 Hz	148.62 μW	200 MΩ	This work

4 Parametric analyses

In section 3, it is proven that the impact mechanism can enhance the efficiency of harvesting energy from the intrawell oscillation. To illustrate whether this advantage exists in a wide range of conditions, the effects of system parameters on the output performance of the SIBTENG are studied in this section. Numerical simulations are carried to obtain the peak power and RMS power in numerous cases of parameters, and the RMS power growth rate are calculated to evaluate the

improvement of energy harvesting by employing the SIBTENG.

4.1 Effect of the distance between the flexible beam and the proof mass

As mentioned earlier, the distance X between the flexible beam and proof mass can significantly influence the mechanical behaviour of the bistable structure of the SIBTENG, and thus it should be a key parameter for achieving desired output performance. The effects of the distance X on the output performance are studied, when A=0.8 G, D_R=0.025 m and μ=0.22, as shown in Fig. 8.

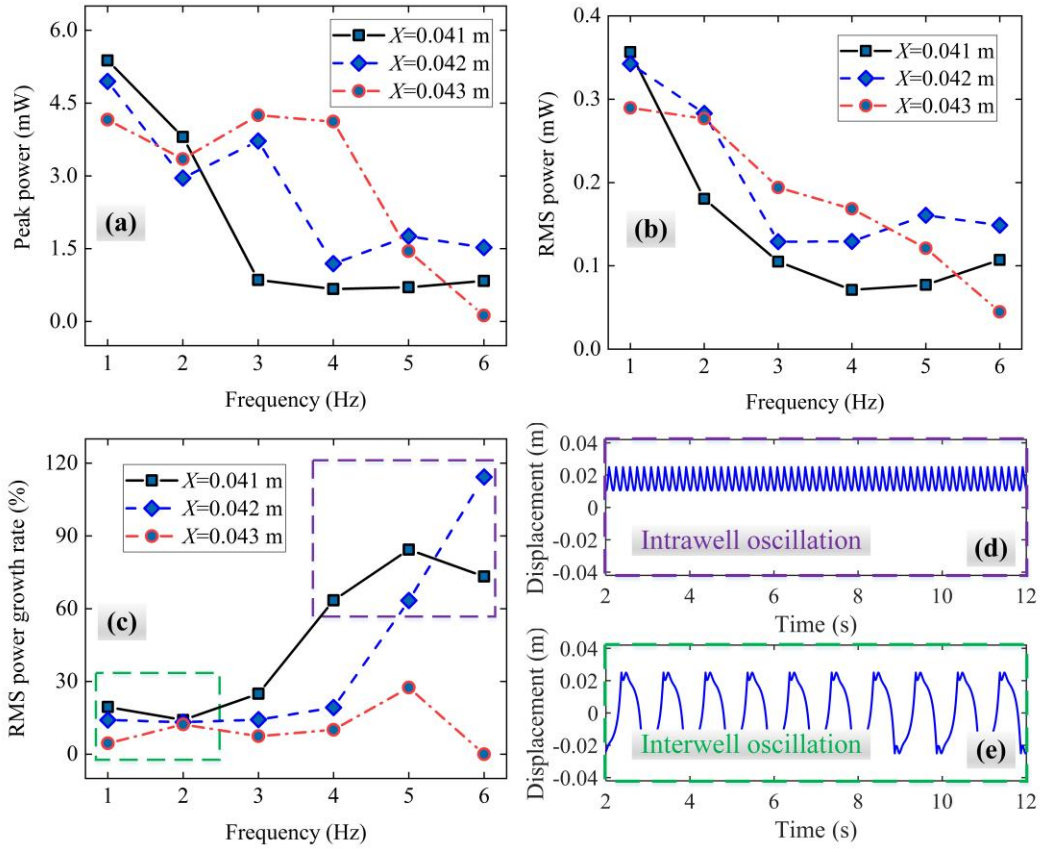

Fig. 8 Effects of the distance between the flexible beam and proof mass on the output performance. (a) Influence of different distances of X on the output peak power; (b) comparison of RMS power with different distances of X; (c) growth rate of RMS power varying with the distance between two flexible beams; (d, e) dynamic behaviours of the SIBTENG.

From Fig. 8a, one can find that the variation trend of the peak power has little difference at 1 Hz and 2 Hz, since the interwell oscillation is the dominant motion

pattern of the proof mass at these frequencies. When the frequency is 3 Hz, the potential barrier increases as the distance X is decreased. Note that there is an increase in the peak power, whereas a sudden drop of the RMS power appears as the excitation frequency increases from 2 Hz to 3 Hz for X=0.042 m or X=0.043 m. This is because the motion pattern of the proof mass is aperiodic interwell oscillation at 3 Hz, and thus the peak motion amplitude is higher and the RMS motion amplitude is lower than those in the case of 2 Hz. Especially, the proof mass is unable to cross the barrier as the distance X is reduced to 0.041 m and thus the motion pattern changes from the interwell oscillation to the intrawell one. Therefore, the peak power in the case of X =0.041 m is much lower than that in the case of X=0.042 m or X=0.043 m.

Moreover, the proof mass cannot cross the potential barrier at 4 Hz as the distance X is 0.042 or 0.041 m, and thus the peak power is lower than that at 3 Hz. As shown in the cases of 5 Hz and 6 Hz, the peak powers are notably reduced regardless of the distance X, owing to the small-amplitude intrawell oscillation. It should be noted that in the case of X=0.043 m at 6 Hz, the oscillation amplitude of the proof mass is quite small and no impact event occurs between the slider and the right stopper, leading to the lowest output peak voltage. Additionally, Fig. 8b depicted the comparison of RMS power for different distances X. Clearly, the variation trend of the RMS power for different distances X is in line with that of the peak power.

To further evaluate the effect of impact mode on the performance of the SIBTENG, Fig. 8c shows the growth rate of the RMS power with the distance X. When the frequency is 6 Hz, the electrical output generated by the sliding mode of the SIBTENG with a distance X of 0.041 m is more than that with a distance X=0.042 m, whereas the output voltage generated by the impact mode of the SIBTENG in the case of X=0.041 m is lower than that of X=0.042 m. Therefore, the RMS power growth rate of X=0.042 m is larger than that of X=0.041 m. Note that no impact event happens between the slider and right stopper in the case of X=0.043 m, and thus the RMS power growth rate is equal to zero. In addition, a clear trend can be seen that the RMS power growth rate rises as the frequency increases. Obviously, in the range from 4 Hz to 6 Hz, the proof mass exhibits intrawell oscillation (Fig. 8d) and the RMS power

growth rate can reach about 60%-120%, owing to the additional power generated by the impact mode. However, in the range from 1 Hz to 3 Hz, the system undergoes interwell oscillation, and the RMS power growth rate is only about 4%-25%. Clearly, under interwell oscillation, the power induced by the impact mode is lower than that by the sliding mode. Consequently, the impact mode in the SIBTENG can hardly improve energy harvesting from interwell oscillation, but it enables high-efficiency energy harvesting from intrawell oscillation.

4.2 Effect of the excitation level

Usually, the excitation is one of the important factors affecting the dynamic behaviours of a bistable system. Fig. 9 demonstrates the effects of the excitation amplitude on the output performance of the SIBTENG, when X=0.042 m, D_R=0.025 m and μ=0.22. As depicted in Fig. 9a, when the excitation amplitude is 0.5 G, the peak power decreases as the frequency increases, and a steep decline of the peak voltage can be observed when the frequency shifts from 1 Hz to 2 Hz. It can be attributed to the change of motion pattern from large-amplitude interwell oscillation (Fig. 9b-I) to small-amplitude intrawell oscillation (Fig. 9b-III). Additionally, when the excitation amplitude increases to 0.7 G or 0.9 G, the displacement amplitude of the proof mass is larger than that in the case of 0.5 G, and thus a higher peak power is achieved at each frequency. Especially, the peak power at 3 Hz in the case of 0.7 G or 0.9 G is much greater than that of 0.5 G. This is because the proof mass can easily cross the potential barrier when the excitation amplitude is 0.7 G or 0.9 G, and the motion of the proof mass is dominated by aperiodic interwell oscillation (Fig. 9b-II).

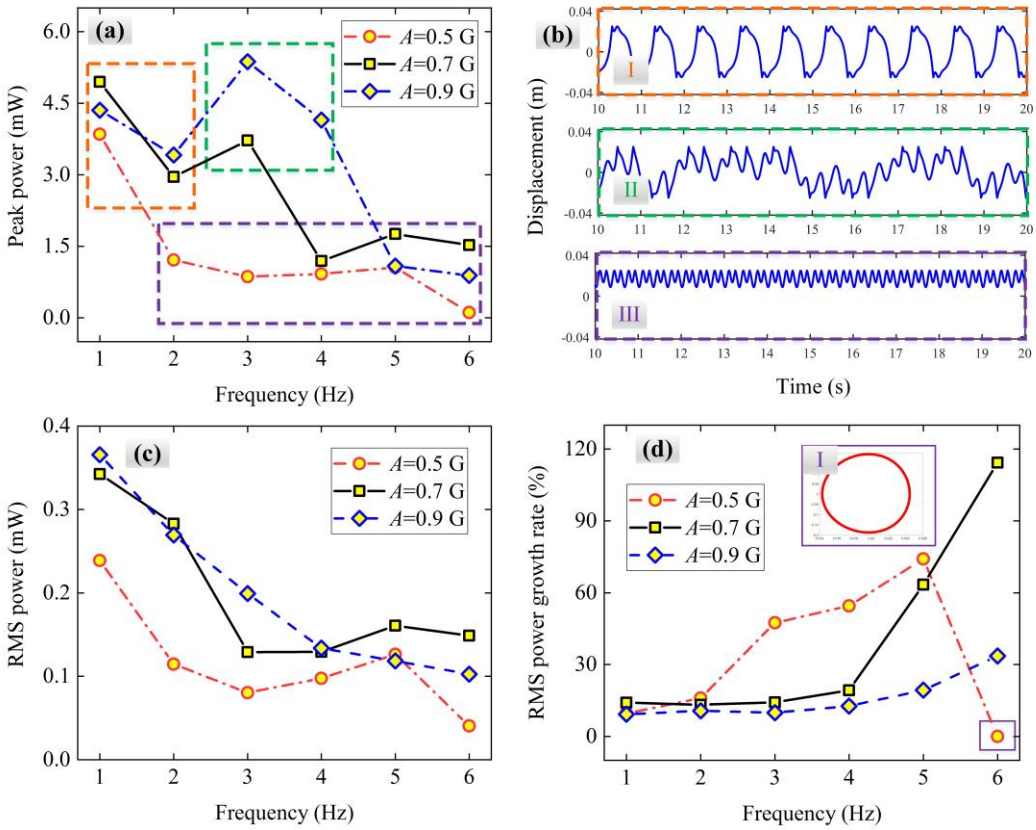

Fig. 9 Effects of the excitation amplitude on the output performance. (a) Influence of excitation amplitude on output peak power; (b) dynamic behaviours of the SIBTENG; (c) comparison of RMS power under an excitation with different amplitudes; (d) growth rate of RMS power with excitation amplitude.

As shown in Fig. 9c, the variation trends of the RMS power with frequency under different excitation amplitudes are almost the same as each other. That is, the RMS power declines as the frequency increases. To evaluate the effect of the impact mode on the output performance, the growth rate of RMS power varying with the excitation amplitude is depicted in Fig. 9d. Clearly, the RMS power growth rate upsurges as the frequency increases, and it increases at most frequencies as the excitation amplitude declines. However, the RMS power growth rate suddenly drops to zero at 6 Hz when the excitation amplitude is 0.5 G. It is because no impact event happens between the slider and right stopper under the small-amplitude excitation, as shown in Fig. 9d-I. Therefore, the impact mode is essential for the SIBTENG to

achieve high-efficient output performance when it undergoes intrawell oscillation.

4.3 Effect of the distance between two stoppers

In the SIBTENG system, the distance between two stoppers determines whether impact events happen between the slider and stoppers. Therefore, the distance D_s also has considerable influence on the dynamic behaviours of the system and the electrical output performance of the SIBTENG. Fig. 10a depicts the peak power for different distances D_s. Clearly, the peak power declines as the frequency increases, in the case of D_s=0.028 m. The peak powers at 1 Hz-3 Hz are much higher than those at 4 Hz-6 Hz, since the motion of the proof mass is large-amplitude interwell oscillation at 1 Hz-3 Hz but small-amplitude intrawell oscillation at 4 Hz-6 Hz. As the distance D_s decreases to 0.025 m, the peak powers at 1 Hz-3 Hz are still high owing to interwell oscillation but low at 4 Hz-5 Hz due to intrawell motion. Note that the motion pattern turns from large-amplitude interwell oscillation to small-amplitude interwell oscillation as the distance D_s decreases from 0.028 m to 0.025 m at the frequencies from 1 Hz to 3 Hz, leading to remarkable reduction of peak powers. Moreover, the impact event between the slider and right stopper happens at the frequencies of 5 Hz and 6 Hz when the distance D_s is 0.025 m, but it does not happen when D_s=0.028. Hence, the peak powers at 5 Hz and 6 Hz in the case of D_s=0.025 m are higher than those of 0.028 m. When the distance D_s is further decreased to 0.022 m, the peak power at each frequency declines further, owing to the reduction in the response amplitude of the proof mass as the distance D_s decreases.

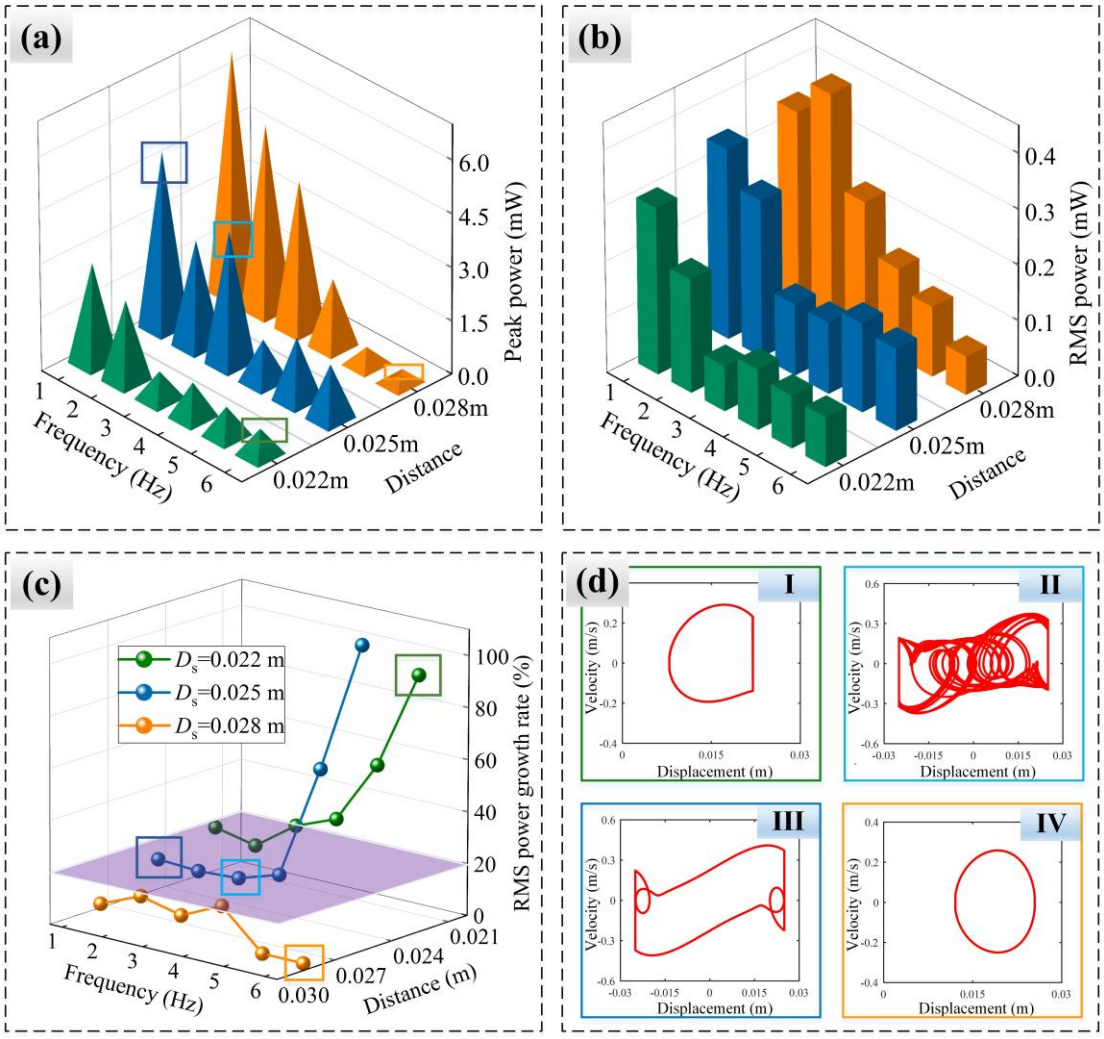

Fig. 10 Effects of the distance between two stoppers on the output performance. (a) Output peak power; (b) RMS power; (c) growth rate of RMS power; and (d) phase portraits for different dynamic behaviours of the SIBTENG.

Fig. 10b shows the RMS power for different distances D_s. Obviously, the variation trend of the RMS power with the distance D_s is similar to that of the peak power. However, unlike the peak power, the RMS power at 3 Hz is lower than that at 2 Hz when the distance D_s is 0.025 m. The reason is that the proof mass experiences aperiodic interwell oscillation with large amplitude at 3 Hz. Fig. 10c demonstrates the growth rate of RMS power varying with the distance D_s. Clearly, the RMS power growth rate increases with the increase of frequency when the distance D_s is 0.022 m or 0.025 m. The maximum RMS power growth rate can reach about 100%, as framed by green box in Fig. 10c. In this scenario, the intrawell oscillation is the predominant

motion pattern of the proof mass, as illustrated in Fig. 10d-I, giving rise to a lower electrical output of the sliding mode than that of the impact mode. Nevertheless, when the motions of the proof mass are aperiodic interwell oscillation (Fig. 10d-II) or periodic interwell one (Fig. 10d-III), the RMS power growth rate is low. Furthermore, in the case of D_s=0.028 m, no impact events appear at 5 Hz and 6 Hz, as shown in Fig. 10d-IV, and thus the RMS power growth rate is equal to zero. Therefore, the impact event more easily happens by narrowing the gap between two stoppers, which is benefit to improve the output performance of the SIBTENG when the motion is dominated by intrawell oscillation.

4.4 Effect of the friction

Friction is also a significant factor which can affect the dynamic responses of the SIBTENG. Thus, the effects of the kinetic friction coefficient between two membranes on the output performance are investigated, as depicted in Fig. 11. When the kinetic friction coefficient is small (i.e., μ=0.14), the inertia force of the proof mass is larger than the friction force, and the proof mass can cross the potential barrier. Therefore, the proof mass undergoes interwell oscillation at most frequencies, leading to large peak powers in the range from 1 Hz to 4 Hz, as shown in Fig. 11a. However, the motion of the proof mass turns from periodic interwell oscillation to aperiodic one at the frequency of 5 Hz, leading to a sudden increase of the peak power. As the frequency continues to increase to 6 Hz, the inertia force becomes so small that the proof mass cannot cross the potential barrier. The motion pattern of the system is thereby dominated by intrawell oscillation, which results in quite low peak power. Furthermore, when the kinetic friction coefficient increases to 0.22, the variation trend of the peak power is similar to the case of μ=0.14. Nevertheless, a sudden decline of the peak power is observed as the frequency moves from 3 Hz to 4 Hz, owing to the decreased inertia force. As the kinetic friction coefficient is further increased (i.e., μ=0.30), the friction force increases, and the proof mass is unable to cross the potential barrier in the range from 3 Hz to 6 Hz. Therefore, the peak powers are low in

this range.

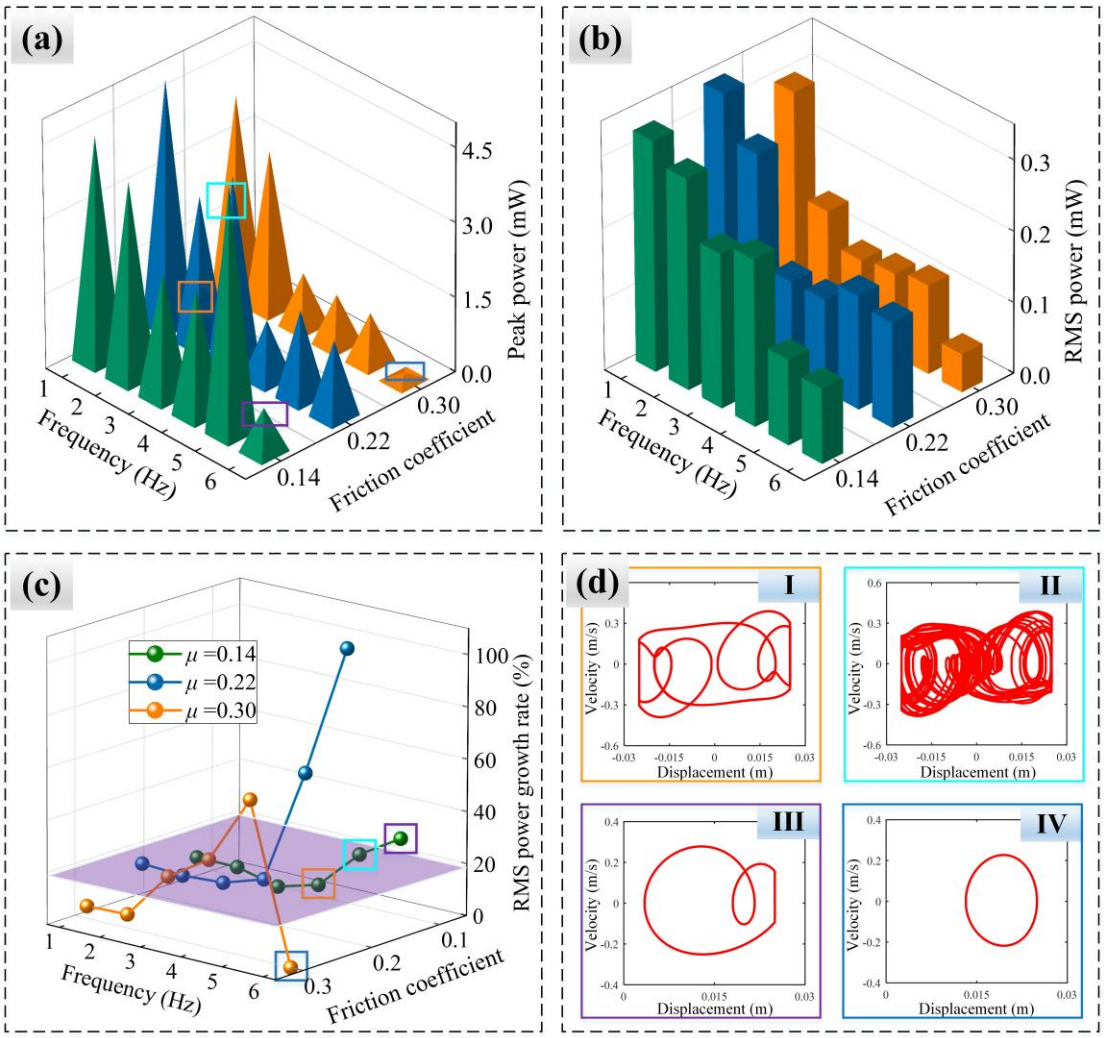

Fig. 11 Effects of the friction between two membranes on the output performance. (a) Output peak power; (b) RMS power; (c) growth rate of the RMS power; (d) phase portraits for different dynamic behaviours of the SIBTENG.

Fig. 11b shows the RMS power for different kinetic friction coefficients. Clearly, the variation trend of the RMS power is similar to that of the peak power. The RMS power growth rate is calculated to evaluate the effect of the kinetic friction coefficient on the output performance of the SIBTENG, as depicted in Fig. 11c. When the kinetic friction coefficient is small (i.e., μ=0.14), the RMS growth rate rises as the frequency increases. Obviously, the RMS growth rate is less than 20% in the frequency region of 1 Hz-4 Hz. This is because the electrical output generated by the sliding mode is

much higher than that by the impact mode when the motion pattern of the proof mass is periodic interwell oscillation, as shown in Fig. 11d-I. Nevertheless, the motion pattern changes into aperiodic interwell oscillation as the frequency increases to 5 Hz, as shown in Fig. 11d-II, resulting in a decrease in electrical output of the sliding mode but an increase of the impact mode. The RMS power growth rate, therefore, exhibits an obvious increasing trend. As the proof mass cannot cross potential barrier at 6 Hz, the electrical output of sliding mode is much lower than that of impact mode, and a growth rate about 40% for the RMS power is achieved. Moreover, when the kinetic friction coefficient increases to 0.22 and 0.3, the friction force increases, and the motion pattern of the proof mass is dominated by intrawell oscillation at most frequencies. The maximum RMS power growth rate reaches about 100% in the case of μ=0.22 at 6 Hz. Nevertheless, the RMS power growth rate falls to zero at 6 Hz when the kinetic friction coefficient is 0.3. The reason is that in such a case, the intrawell oscillation is so weak that the slider never impacts with the stopper, as shown in Fig. 11d-IV, and thus the impact mode has no contribution to energy harvesting.

5 Experiments

To evaluate the output performance of the SIBTENG, the experiments are investigated in this section. The experimental output voltages generated by the impact mode and the sliding mode are measured. In addition, and the RMS power and the growth rate are calculated to evaluate the improvement of energy harvesting by introducing the impact mode.

5.1 Experimental setup

Fig. 12 shows the experimental setup used to measure the output performance of the SIBTENG. In the experimental setup, the SIBTENG is fixed to a shake table (MPA406/M232A), which is utilized to provide low-frequency base excitations. When the SIBTENG is in operating state, the electrical output performance is

measured by an oscilloscope (Micsig TO1104). In the experiments, the amplitude and frequency of the acceleration excitation are 0.8 G and 5 Hz, respectively. The mass of slider is 0.0053 kg, and the sizes of the FEP membranes are 0.04 m × 0.016 m for the impact mode and 0.05 m × 0.016 m for the sliding mode. The load resistance is 90 MΩ.

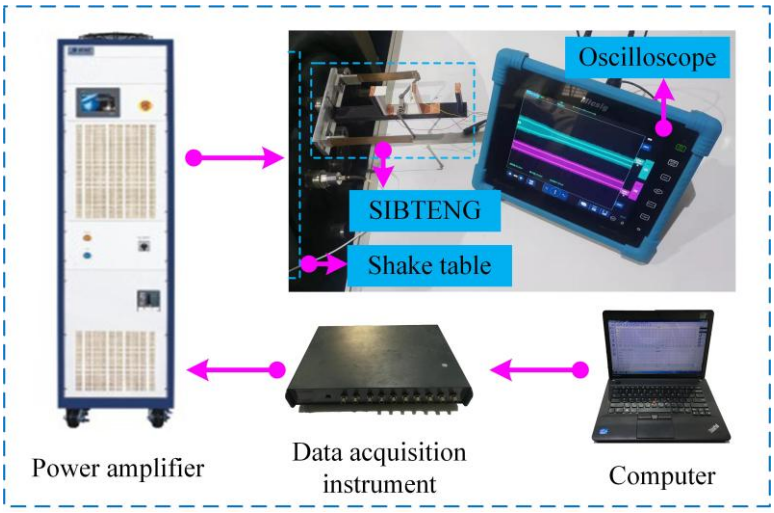

Fig. 12 Experimental setup for evaluating the electrical output performance of the SIBTENG

5.2 Electrical output performance of the SIBTENG

The experimental output voltages generated by the impact mode and the sliding mode are measured, separately, which are also compared with the theoretical results, as shown in Fig. 13. Note that the kinetic friction coefficient used for theoretical predictions is 0.47, and the motion pattern of the proof mass is intrawell oscillation in this case. Comparison between the theoretical and experimental output voltages induced by the impact mode is shown in Fig. 13a. Clearly, there is high consistency between the theoretical result and the experimental result of voltage response. For the sliding mode, the voltage amplitude of theoretical prediction matches well with the experimental result, as seen in Fig. 13b, whereas the shapes of the voltage signals are inconsistent with each other, owing to the effect of the machining and assembly errors on the experiment results. On the whole, the theoretical and experimental voltage responses are consistent for both the sliding and impact modes.

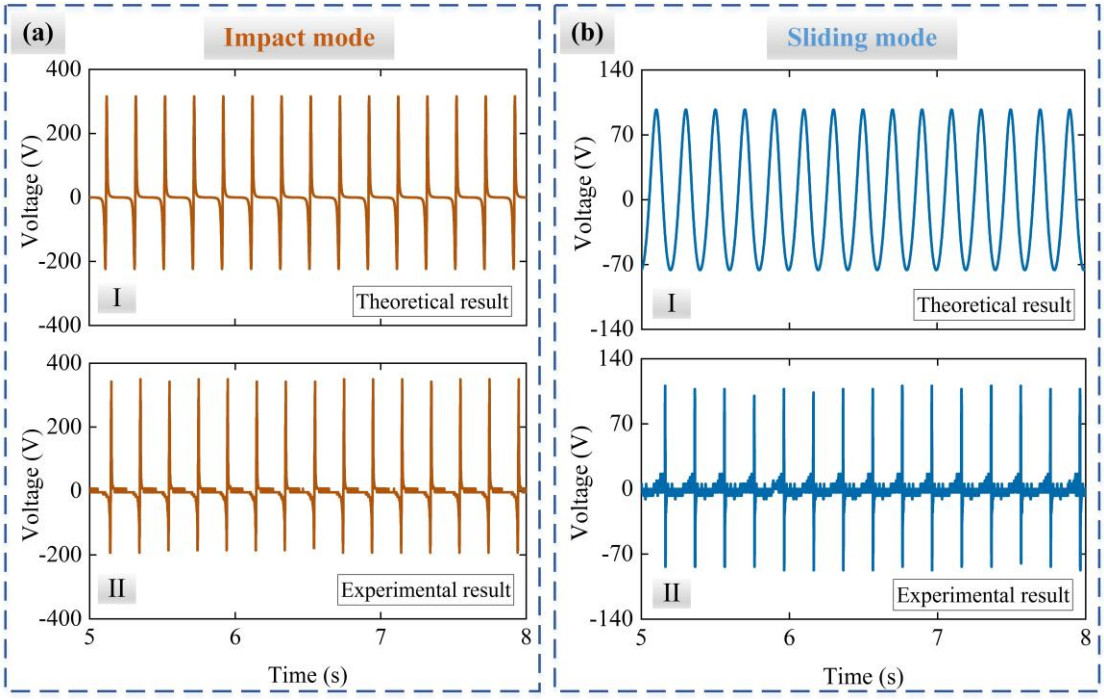

Fig. 13 Theoretical and experimental results at A=0.8 G, f =5 Hz, μ=0.47, m_s=0.0053 kg, l_s=0.05 m, w_{FEP}=0.016 m and R=90 MΩ. (a) Output voltage with impact mode: (I) theoretical result, (II) experimental result; (b) electrical response with sliding mode: (I) theoretical result, (II) experimental result.

To validate the electrical output performance of the SIBTENG, the voltage is measured in the frequency range from 4 Hz to 6 Hz, where the SIBTENG undergoes intrawell oscillation. The RMS power and the growth rate varying with the excitation frequency are calculated based on the measured voltages, as depicted in Fig. 14. It can be observed that both the RMS voltage and RMS power declines as the frequency increases, and the RMS voltage generated by the impact mode is greater than that by the sliding mode. From Fig. 14b, one also can see that the RMS power growth rates can be improved from about 105% to 210% as the frequency increases from 4 Hz to 6 Hz. This variation trend matches well with the theoretical prediction discussed in Section 3. It should be noted that the RMS power growth rate obtained by the experiments is larger than that in the case of numerical simulations. This is because the machining and assembly errors in experiments could induce a discrepancy between the experimental and numerical output performance for the sliding mode, as

shown in Fig. 13b. Specifically, both the experimental RMS voltage and RMS power of the sliding mode is lower than the numerical ones. However, the numerical simulations match well with the experimental tests for the impact mode. Consequently, the experimental RMS power growth rate is larger than the numerical one. Importantly, remarkable growth rates (>100%) of the RMS power are fulfilled by the impact mode. Therefore, the impact mode can effectively improve the efficiency of harvesting energy from intrawell oscillation.

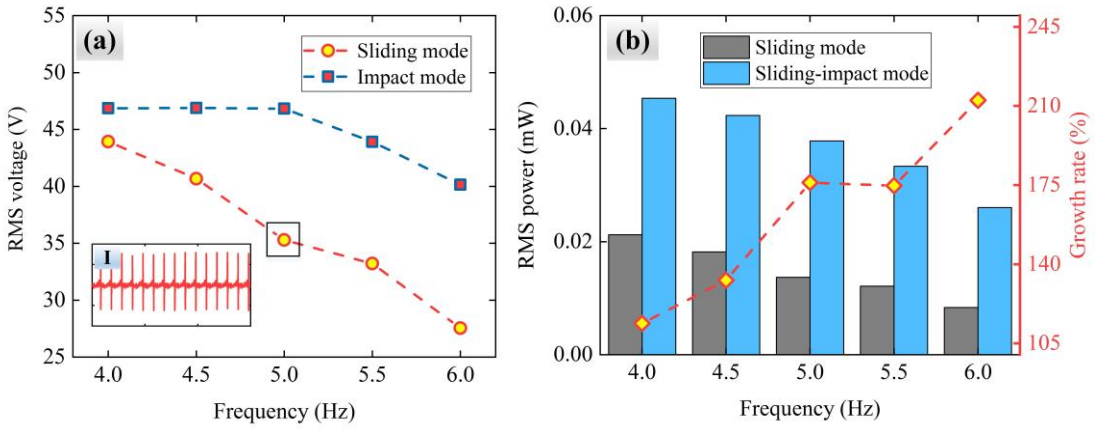

Fig. 14 Output performance of the SIBTENG (a) RMS voltage under different frequencies; (b) RMS power and the growth rate.

6 Conclusions

In this paper, a sliding-impact bistable triboelectric nanogenerator (SIBTENG) is proposed to enhance the efficiency of harvesting energy from low-frequency intrawell oscillation. This proposed SIBTENG harvest vibration energy by combining the sliding-mode and impact-mode mechanisms of power generation. The impact mode is effective to harvest energy from intrawell oscillation once the proof mass cannot cross the potential energy barrier. In such a case, the output performance can be increased by more than 100% owing to the impact mode, which is a substantial improvement over the traditional sliding-mode bistable TENG (SBTENG). In addition, the effects of system parameters, including the distance between the flexible beam and proof mass, the excitation amplitude, the distance between two stoppers and the friction, on

the output performance are investigated. It indicates that the SIBTENG always outperforms the conventional SBTENG in a wide range of parameters when the motion pattern of the proof mass is dominated by intrawell oscillation. Finally, experiments are conducted to evaluate the output performance of the SIBTENG, which validates the benefit induced by the impact mode. Hence, this study presents a new method to enhance the efficiency of harvesting energy from low-frequency intrawell oscillation by introducing the impact mode into the traditional SBTENG.

Declaration of Competing Interest

The authors declare that they have no known competing financial interests or personal relationships that could have appeared to influence the work reported in this paper.

Acknowledgments

This research work was supported by National Natural Science Foundation of China (12122206, 11972152, and 12002122), Natural Science Foundation of Hunan Province (2020JJ4208, 2021JJ40092) and Natural Science Foundation of Chongqing (cstc2021jcyj-msxmX0461).

References

[1] C. Lan, G. Hu, Y. Liao, W. Qin, A wind-induced negative damping method to achieve high-energy orbit of a nonlinear vibration energy harvester, Smart Mater. Struct. 30 (2021) 02LT02. https://doi.org/10.1088/1361-665X/abd962.

[2] H. Tian, X. Shan, H. Cao, T. Xie, Enhanced performance of airfoil-based piezoaeroelastic energy harvester: numerical simulation and experimental verification, Mech. Syst. Signal Process. 162 (2022) 108065. https://doi.org/10.1016/j.ymssp.2021.108065.

[3] C.L. Zhang, Z.H. Lai, M.Q. Li, D. Yurchenko, Wind energy harvesting from a conventional

turbine structure with an embedded vibro-impact dielectric elastomer generator, J. Sound Vib. 487 (2020) 115616. https://doi.org/10.1016/j.jsv.2020.115616.

[4] Z.H. Lin, G. Cheng, S. Lee, K.C. Pradel, Z.L. Wang, Harvesting water drop energy by a sequential contact-electrification and electrostatic-induction process, Adv. Mater. 26 (2014) 4690–4696. https://doi.org/10.1002/adma.201400373.

[5] S.F. Nabavi, A. Farshidianfar, A. Afsharfard, H.H. Khodaparast, An ocean wave-based piezoelectric energy harvesting system using breaking wave force, Int. J. Mech. Sci. 151 (2019) 498–507. https://doi.org/10.1016/j.ijmecsci.2018.12.008.

[6] G. Sui, X. Shan, H. Tian, L. Wang, T. Xie, Study on different underwater energy harvester arrays based on flow-induced vibration, Mech. Syst. Signal Process. 167 (2022) 108546. https://doi.org/10.1016/j.ymssp.2021.108546.

[7] B. Qin, Y. Chen, Z. Chen, L. Zuo, Modeling, bench test and ride analysis of a novel energy-harvesting hydraulically interconnected suspension system, Mech. Syst. Signal Process. 166 (2022) 108456. https://doi.org/10.1016/j.ymssp.2021.108456.

[8] X. Mei, S. Zhou, Z. Yang, T. Kaizuka, K. Nakano, A tri-stable energy harvester in rotational motion: Modeling, theoretical analyses and experiments, J. Sound Vib. 469 (2020) 115142. https://doi.org/10.1016/j.jsv.2019.115142.

[9] Z.Q. Lu, H. Ding, L.Q. Chen, Resonance response interaction without internal resonance in vibratory energy harvesting, Mech. Syst. Signal Process. 121 (2019) 767–776. https://doi.org/10.1016/j.ymssp.2018.11.035.

[10] J. Wang, L. Geng, S. Zhou, Z. Zhang, Z. Lai, D. Yurchenko, Design, modeling and experiments of broadband tristable galloping piezoelectric energy harvester, Acta Mech. Sin. Xuebao. 36 (2020) 592–605. https://doi.org/10.1007/s10409-020-00928-5.

[11] J. Zhou, X. Zhao, K. Wang, Y. Chang, D. Xu, G. Wen, Bio-inspired bistable piezoelectric vibration energy harvester: Design and experimental investigation, Energy. 228 (2021) 120595. https://doi.org/10.1016/j.energy.2021.120595.

[12] S. Touairi, M. Mabrouki, Control and modelling evaluation of a piezoelectric harvester system, Int. J. Dyn. Control. 9 (2021) 1559–1575. https://doi.org/10.1007/s40435-021-00764-w.

[13] S. Touairi, M. Mabrouki, Chaotic dynamics applied to piezoelectric harvester energy prediction with time delay, Int. J. Dyn. Control. 10 (2022) 699–720.

https://doi.org/10.1007/s40435-021-00837-w.

[14] F.M. Foong, C.K. Thein, B.L. Ooi, D. Yurchenko, Increased power output of an electromagnetic vibration energy harvester through anti-phase resonance, Mech. Syst. Signal Process. 116 (2019) 129–145. https://doi.org/10.1016/j.ymssp.2018.06.012.

[15] H. Zhang, L.R. Corr, T. Ma, Effects of electrical loads containing non-resistive components on electromagnetic vibration energy harvester performance, Mech. Syst. Signal Process. 101 (2018) 55–66. https://doi.org/10.1016/j.ymssp.2017.08.031.

[16] M. Xie, D. Zabek, C. Bowen, M. Abdelmageed, M. Arafa, Wind-driven pyroelectric energy harvesting device, Smart Mater. Struct. 25 (2016). https://doi.org/10.1088/0964-1726/25/12/125023.

[17] J. Luo, Z. Wang, L. Xu, A.C. Wang, K. Han, T. Jiang, Q. Lai, Y. Bai, W. Tang, F.R. Fan, Z.L. Wang, Flexible and durable wood-based triboelectric nanogenerators for self-powered sensing in athletic big data analytics, Nat. Commun. 10 (2019) 5147. https://doi.org/10.1038/s41467-019-13166-6.

[18] L. Zhang, B. Meng, Y. Xia, Z. Deng, H. Dai, P. Hagedorn, Z. Peng, L. Wang, Galloping triboelectric nanogenerator for energy harvesting under low wind speed, Nano Energy. 70 (2020) 104477. https://doi.org/10.1016/j.nanoen.2020.104477.

[19] F.R. Fan, Z.Q. Tian, Z. Lin Wang, Flexible triboelectric generator, Nano Energy. 1 (2012) 328–334. https://doi.org/10.1016/j.nanoen.2012.01.004.

[20] L. Zhou, D. Liu, Z. Zhao, S. Li, Y. Liu, L. Liu, Y. Gao, Z.L. Wang, J. Wang, Simultaneously Enhancing Power Density and Durability of Sliding-Mode Triboelectric Nanogenerator via Interface Liquid Lubrication, Adv. Energy Mater. 10 (2020) 2002920. https://doi.org/10.1002/aenm.202002920.

[21] S. Wang, L. Lin, Y. Xie, Q. Jing, S. Niu, Z.L. Wang, Sliding-triboelectric nanogenerators based on in-plane charge-separation mechanism, Nano Lett. 13 (2013) 2226–2233. https://doi.org/10.1021/nl400738p.

[22] X. Liang, T. Jiang, G. Liu, T. Xiao, L. Xu, W. Li, F. Xi, C. Zhang, Z.L. Wang, Triboelectric Nanogenerator Networks Integrated with Power Management Module for Water Wave Energy Harvesting, Adv. Funct. Mater. 29 (2019) 1807241. https://doi.org/10.1002/adfm.201807241.

[23] Y. Fu, H. Ouyang, R.B. Davis, Triboelectric energy harvesting from the vibro-impact of three

cantilevered beams, Mech. Syst. Signal Process. 121 (2019) 509–531. https://doi.org/10.1016/j.ymssp.2018.11.043.

[24] Y. Fu, H. Ouyang, R.B. Davis, Nonlinear dynamics and triboelectric energy harvesting from a three-degree-of-freedom vibro-impact oscillator, Nonlinear Dyn. 92 (2018) 1985–2004. https://doi.org/10.1007/s11071-018-4176-3.

[25] S. Niu, S. Wang, L. Lin, Y. Liu, Y.S. Zhou, Y. Hu, Z.L. Wang, Theoretical study of contact-mode triboelectric nanogenerators as an effective power source, Energy Environ. Sci. 6 (2013) 3576–3583. https://doi.org/10.1039/c3ee42571a.

[26] S. Wang, Y. Xie, S. Niu, L. Lin, Z.L. Wang, Freestanding triboelectric-layer-based nanogenerators for harvesting energy from a moving object or human motion in contact and non-contact modes, Adv. Mater. 26 (2014) 2818–2824. https://doi.org/10.1002/adma.201305303.

[27] S. Niu, Y. Liu, X. Chen, S. Wang, Y.S. Zhou, L. Lin, Y. Xie, Z.L. Wang, Theory of freestanding triboelectric-layer-based nanogenerators, Nano Energy. 12 (2015) 760–774. https://doi.org/10.1016/j.nanoen.2015.01.013.

[28] T. Jiang, X. Chen, C.B. Han, W. Tang, Z.L. Wang, Theoretical study of rotary freestanding triboelectric nanogenerators, Adv. Funct. Mater. 25 (2015) 2928–2938. https://doi.org/10.1002/adfm.201500447.

[29] Y. Yang, H. Zhang, J. Chen, Q. Jing, Y.S. Zhou, X. Wen, Z.L. Wang, Single-electrode-based sliding triboelectric nanogenerator for self-powered displacement vector sensor system, ACS Nano. 7 (2013) 7342–7351. https://doi.org/10.1021/nn403021m.

[30] B. Meng, W. Tang, Z.H. Too, X. Zhang, M. Han, W. Liu, H. Zhang, A transparent single-friction-surface triboelectric generator and self-powered touch sensor, Energy Environ. Sci. 6 (2013) 3235–3240. https://doi.org/10.1039/c3ee42311e.

[31] Y. Yang, H. Zhang, Z.H. Lin, Y.S. Zhou, Q. Jing, Y. Su, J. Yang, J. Chen, C. Hu, Z.L. Wang, Human skin based triboelectric nanogenerators for harvesting biomechanical energy and as self-powered active tactile sensor system, ACS Nano. 7 (2013) 9213–9222. https://doi.org/10.1021/nn403838y.

[32] S. Niu, Y. Liu, S. Wang, L. Lin, Y.S. Zhou, Y. Hu, Z.L. Wang, Theory of sliding-mode triboelectric nanogenerators, Adv. Mater. 25 (2013) 6184–6193.

https://doi.org/10.1002/adma.201302808.

[33] Y. Fu, H. Ouyang, R. Benjamin Davis, Nonlinear structural dynamics of a new sliding-mode triboelectric energy harvester with multistability, Nonlinear Dyn. 100 (2020) 1941–1962. https://doi.org/10.1007/s11071-020-05645-z.

[34] Y. Wu, J. Qu, P.K. Chu, D.M. Shin, Y. Luo, S.P. Feng, Hybrid photovoltaic-triboelectric nanogenerators for simultaneously harvesting solar and mechanical energies, Nano Energy. 89 (2021) 106376. https://doi.org/10.1016/j.nanoen.2021.106376.

[35] F. Zheng, Y. Sun, X. Wei, J. Chen, Z. Yuan, X. Jin, L. Tao, Z. Wu, A hybridized water wave energy harvester with a swing magnetic structure toward intelligent fishing ground, Nano Energy. 90 (2021) 106631. https://doi.org/10.1016/j.nanoen.2021.106631.

[36] Q. Zheng, Y. Zou, Y. Zhang, Z. Liu, B. Shi, X. Wang, Y. Jin, H. Ouyang, Z. Li, Z.L. Wang, Biodegradable triboelectric nanogenerator as a life-time designed implantable power source, Sci. Adv. 2 (2016) 1501478. https://doi.org/10.1126/sciadv.1501478.

[37] B. Cheng, Q. Xu, Y. Ding, S. Bai, X. Jia, Y. Yu, J. Wen, Y. Qin, High performance temperature difference triboelectric nanogenerator, Nat. Commun. 12 (2021) 4782. https://doi.org/10.1038/s41467-021-25043-2.

[38] J.S. Kim, J. Kim, J.N. Kim, J. Ahn, J.H. Jeong, I. Park, D. Kim, I.K. Oh, Collectively Exhaustive Hybrid Triboelectric Nanogenerator Based on Flow-Induced Impacting-Sliding Cylinder for Ocean Energy Harvesting, Adv. Energy Mater. 12 (2021) 2103076. https://doi.org/10.1002/aenm.202103076.

[39] H. Kim, Q. Zhou, D. Kim, I.K. Oh, Flow-induced snap-through triboelectric nanogenerator, Nano Energy. 68 (2020) 104379. https://doi.org/10.1016/j.nanoen.2019.104379.

[40] C. Rodrigues, D. Nunes, D. Clemente, N. Mathias, J.M. Correia, P. Rosa-Santos, F. Taveira-Pinto, T. Morais, A. Pereira, J. Ventura, Emerging triboelectric nanogenerators for ocean wave energy harvesting: State of the art and future perspectives, Energy Environ. Sci. 13 (2020) 2657–2683. https://doi.org/10.1039/d0ee01258k.

[41] C. Wu, J.H. Park, B. Koo, X. Chen, Z.L. Wang, T.W. Kim, Capsule Triboelectric Nanogenerators: Toward Optional 3D Integration for High Output and Efficient Energy Harvesting from Broadband-Amplitude Vibrations, ACS Nano. 12 (2018) 9947–9957. https://doi.org/10.1021/acsnano.8b03824.

[42] S. Cho, Y. Yun, S. Jang, Y. Ra, J.H. Choi, H.J. Hwang, D. Choi, D. Choi, Universal biomechanical energy harvesting from joint movements using a direction-switchable triboelectric nanogenerator, Nano Energy. 71 (2020) 104584. https://doi.org/10.1016/j.nanoen.2020.104584.

[43] X. Zhang, J. Ai, Y. Yue, Y. Shi, R. Zou, B. Su, Anti-stress ball energy harvester, Nano Energy. 90 (2021) 106493. https://doi.org/10.1016/j.nanoen.2021.106493.

[44] T. Wang, G. Gu, W. Shang, J. Gan, W. Zhang, H. Luo, B. Zhang, P. Cui, J. Guo, F. Yang, G. Cheng, Z. Du, A self-powered photodetector using a pulsed triboelectric nanogenerator for actual working environments with random mechanical stimuli, Nano Energy. 90 (2021) 106518. https://doi.org/10.1016/j.nanoen.2021.106518.

[45] K.D. Pham, D. Bhatia, N.D. Huynh, H. Kim, J.M. Baik, Z.H. Lin, D. Choi, Automatically switchable mechanical frequency regulator for continuous mechanical energy harvesting via a triboelectric nanogenerator, Nano Energy. 89 (2021) 106350. https://doi.org/10.1016/j.nanoen.2021.106350.

[46] L. Lin, S. Wang, Y. Xie, Q. Jing, S. Niu, Y. Hu, Z.L. Wang, Segmentally structured disk triboelectric nanogenerator for harvesting rotational mechanical energy, Nano Lett. 13 (2013) 2916–2923. https://doi.org/10.1021/nl4013002.

[47] H. Zhao, H. Ouyang, A capsule-structured triboelectric energy harvester with stick-slip vibration and vibro-impact, Energy. 235 (2021) 121393. https://doi.org/10.1016/j.energy.2021.121393.

[48] W. Tang, C.B. Han, C. Zhang, Z.L. Wang, Cover-sheet-based nanogenerator for charging mobile electronics using low-frequency body motion/vibration, Nano Energy. 9 (2014) 121–127. https://doi.org/10.1016/j.nanoen.2014.07.005.

[49] W. Yang, J. Chen, G. Zhu, X. Wen, P. Bai, Y. Su, Y. Lin, Z. Wang, Harvesting vibration energy by a triple-cantilever based triboelectric nanogenerator, Nano Res. 6 (2013) 880–886. https://doi.org/10.1007/s12274-013-0364-0.

[50] Y. Qi, G. Liu, Y. Gao, T. Bu, X. Zhang, C. Xu, Y. Lin, C. Zhang, Frequency band characteristics of a triboelectric nanogenerator and ultra-wide-band vibrational energy harvesting, ACS Appl. Mater. Interfaces. 13 (2021) 26084–26092. https://doi.org/10.1021/acsami.1c06031.

[51] C.-R. Yang, C.-T. Ko, S.-F. Chang, M.-J. Huang, Study on fabric-based triboelectric nanogenerator using graphene oxide/porous PDMS as a compound friction layer, Nano Energy. 92 (2022) 106791. https://doi.org/10.1016/j.nanoen.2021.106791.

[52] M.S. Rasel, P. Maharjan, M. Salauddin, M.T. Rahman, H.O. Cho, J.W. Kim, J.Y. Park, An impedance tunable and highly efficient triboelectric nanogenerator for large-scale, ultra-sensitive pressure sensing applications, Nano Energy. 49 (2018) 603–613. https://doi.org/10.1016/j.nanoen.2018.04.060.

[53] K. Wang, J. Zhou, H. Ouyang, Y. Chang, D. Xu, A dual quasi-zero-stiffness sliding-mode triboelectric nanogenerator for harvesting ultra-low frequency vibration energy, Mech. Syst. Signal Process. 151 (2021) 107368. https://doi.org/10.1016/j.ymssp.2020.107368.

[54] K. Wang, H. Ouyang, J. Zhou, Y. Chang, D. Xu, H. Zhao, A nonlinear hybrid energy harvester with high ultralow-frequency energy harvesting performance, Meccanica. 56 (2021) 461–480. https://doi.org/10.1007/s11012-020-01291-2.

[55] N. Yu, H. Ma, C. Wu, G. Yu, B. Yan, Modeling and experimental investigation of a novel bistable two-degree-of-freedom electromagnetic energy harvester, Mech. Syst. Signal Process. 156 (2021) 107608. https://doi.org/10.1016/j.ymssp.2021.107608.

[56] Y. Fu, H. Ouyang, R.B. Davis, Effects of electrical properties on vibrations via electromechanical coupling in triboelectric energy harvesting, J. Phys. D. Appl. Phys. 53 (2020) 215501. https://doi.org/10.1088/1361-6463/ab7792.

[57] F. Arab Hassani, R.P. Mogan, G.G.L. Gammad, H. Wang, S.C. Yen, N. V. Thakor, C. Lee, Toward Self-Control Systems for Neurogenic Underactive Bladder: A Triboelectric Nanogenerator Sensor Integrated with a Bistable Micro-Actuator, ACS Nano. 12 (2018) 3487–3501. https://doi.org/10.1021/acsnano.8b00303.

[58] H. Deng, J. Ye, Y. Du, J. Zhang, M. Ma, X. Zhong, Bistable broadband hybrid generator for ultralow-frequency rectilinear motion, Nano Energy. 65 (2019) 103973. https://doi.org/10.1016/j.nanoen.2019.103973.

[59] D. Tan, J. Zhou, K. Wang, C. Cai, D. Xu, Modeling and analysis of the friction in a non-linear sliding-mode triboelectric energy harvester, Acta Mech. Sin. 38 (2022) 521330. https://doi.org/10.1007/s10409-022-09013-k.

[60] H. Zhao, H. Ouyang, Theoretical investigation and experiment of a disc-shaped triboelectric

energy harvester with a magnetic bistable mechanism, Smart Mater. Struct. 30 (2021) 095026. https://doi.org/10.1088/1361-665X/ac26a7.

[61] D. Tan, J. Zhou, K. Wang, X. Zhao, Q. Wang, D. Xu, Bow-type bistable triboelectric nanogenerator for harvesting energy from low-frequency vibration, Nano Energy. 92 (2022) 106746. https://doi.org/10.1016/j.nanoen.2021.106746.

[62] Gere J, Goodno B. Mechanics of materials. (2009).

[63] X. Wang, R. Wang, B. Huang, J. Mo, H. Ouyang, A Study of Effect of Various Normal Force Loading Forms on Frictional Stick-Slip Vibration, J. Dyn. Monit. Diagnostics. 1 (2021) 46–55. https://doi.org/10.37965/jdmd.v2i2.48.

[64] H. Zhao, O. Huajiang, Structural and electrical dynamics of a grating-patterned triboelectric energy harvester with stick–slip oscillation and magnetic bistability, Nonlinear Dyn. 109 (2022) 479–506. https://doi.org/10.1007/s11071-022-07230-y.

[65] H. Zhao, H. Ouyang, A vibro-impact triboelectric energy harvester with a magnetic bistable mechanism and grating-patterned films for dual power enhancement, Mech. Syst. Signal Process. 178 (2022) 109318. https://doi.org/10.1016/j.ymssp.2022.109318.

[66] X. Yang, S.K. Lai, C. Wang, J.M. Wang, H. Ding, On a spring-assisted multi-stable hybrid-integrated vibration energy harvester for ultra-low-frequency excitations, Energy. 252 (2022) 124028. https://doi.org/10.1016/j.energy.2022.124028.